Simulation of the forming of tufted multilayer composite preforms

J. Huang, Philippe Boissé, N. Hamila

Version of Record: https://www.sciencedirect.com/science/article/pii/S1359836821003681
Manuscript_ad016154944983092bf059f6befa89d6

Simulation of the forming of tufted multilayer composite preforms

Jin Huang[1], Philippe Boisse[1*], Nahiène Hamila[2]

[1]Université de Lyon, LaMCoS, CNRS, INSA-Lyon, F-69621, France

[2]ENI Brest, UMR CNRS 6027, IRDL, Brest, France

Abstract

Tufting of preforms increases the resistance of the laminated composites to delamination. Draping of the preforms is clearly modified by the presence of tufting threads. A simulation approach for the forming of tufted textile reinforcement stacks is proposed. It determines the state of the tufted preforms after forming and in particular the possible wrinkles. The layers of textile reinforcements are modeled by stress resultant shells. Tufting threads are modeled by rod chains that can slide with friction relative to the textile reinforcements. The geometry of these rod elements is enhanced by a description of Hermite and the bending of the threads is taken into account through the position of neighboring elements. The approach accurately simulates the forming of tufted preforms and in particular the wrinkles that are observed in the forming experiments.

Key words: A. Fabrics/textiles; A. 3-Dimensional reinforcement; C. Finite element analysis (FEA); E. Forming; Tufting

1. Introduction

Laminate composites exhibit good in-plane mechanical properties. Nevertheless, due to their multilayer composition, their resistance to delamination is limited. In order to improve the resistance to delamination and also to impact, Through-the-Thickness Reinforcement techniques (TTR) have been developed. Z-pinning consists of inserting rigid rods into the thickness of the composite before the resin is cured [1,2]. Stitching is another TTR method carried out by one or two needles interlocking one or two threads [3-5]. Tufting is a fairly new and simple technique for dry preforms used in Liquid Composite Moulding (LCM) processes, such as infusion [5-8]. A single needle carries a single thread through the thickness of the laminate. The thread can cross totally or partially through the thickness of the laminate. In the first case a thread loop is formed on the underside. The yarns are not interlocked and are held in

*Corresponding author.
E-mail address: philippe.boisse@insa-lyon.fr (P. Boisse)

contact with the fibrous layers of the laminate by friction.

These TTR techniques have shown, in quite a number of studies, their interest in increasing the resistance to delamination of laminates [1,9-14]. The different TTR techniques presented above have their advantages and disadvantages depending on the nature of the composite part being manufactured [8]. Tufting is best suited for dry fiber preform for LCM processes [6]. It needs access from a single side of the laminate and makes it easier to reinforce a thick stack of composite reinforcements. It is a relatively economical method [5,15]. Tufting is the TTR method that is considered in this work.

Tufting can be carried out on the 3D preform by a tufting head fastened to an articulated robot arm [5]. Depending on the geometry of the preform, this operation can be complex or even challenging. An alternative is to perform the tufting operation on a flat stack of textile reinforcements, which is much simpler and more efficient, and then to shape the tufted laminate to obtain a tufted preform [16]. Relative slippage of the plies is usually necessary for the simultaneous shaping of the laminate when all layers have different orientations. Tufting modifies and reduces these relative slippages but enables them to a certain extent because the threads can slip relative to the textile layers, which makes forming in general possible. The possibility of forming tufted laminates has been investigated experimentally in several studies [16-20]. Through forming experiments, these works have analyzed the feasibility of the process, the role of tufting on the appearance of wrinkles and the influence of the tufting pattern. The physics of this forming is complex because it is the shaping of a multi-layer reinforcement (which is already a complex process [21-23]) which is conditioned by the presence of the tufting threads and their slippage with respect to the textile reinforcements.

The objective of the present study is to propose and validate an approach for the simulation of the forming of tufted laminated textile composites reinforcements. Considering the complexity of the deformation brought by the presence of the tufting threads and their possible slippage, this simulation approach is essential for the manufacturing by forming of tufted preforms. To our knowledge there is no simulation approach for the forming of tufted multi-ply preforms. Simulation methods have been proposed for the forming of stitched textile reinforcements [24-27]. The problem is quite different because the stitches are interlocked and are modeled by links between two given points of two neighboring plies, whereas the tuft can

slip significantly with respect to the multiply preform as will be shown in the examples presented. This article presents the modeling during the forming of the textile layers and most importantly of tuft threads that can slide with respect to the textile plies. Each textile reinforcement ply is modeled by stress resultant shells. Threads are modeled by digital rod chain with the addition of an improvement of the geometry by Hermite interpolation and a bending stiffness by using the position of the neighboring elements. The contact of the thread with the textile layers with sliding and friction is modeled by a penalty approach and a "stick and slip" model which allows for large thread slippage through the textile reinforcement. Two models of the tufting threads, taking into account or not the connection between the neighboring tufts are considered. The simulation results obtained by the proposed simulation approach are compared to experimental results in hemispherical forming and square box forming. Wrinkling development is also analyzed and compared. Formings with and without tufting are also discussed to see the consequences of tufting on the forming process.

2. Tufting process and tufted composite reinforcements

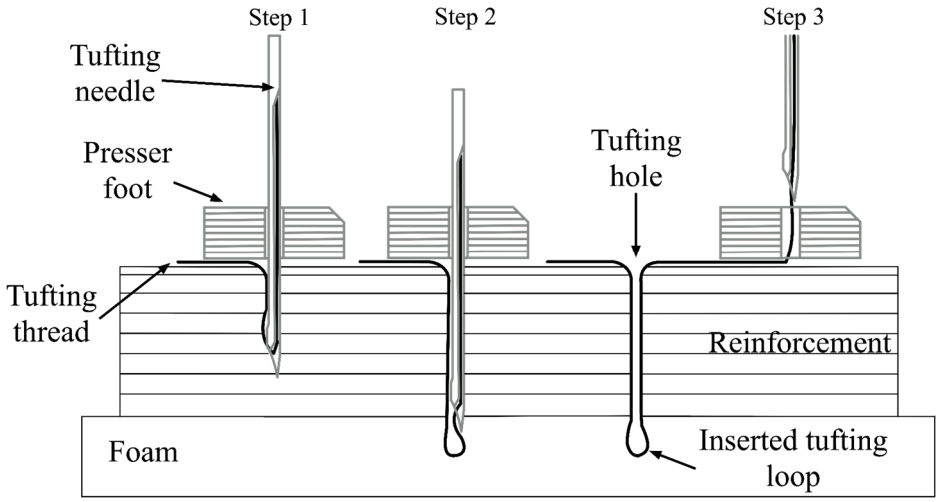

Fig.1 Manufacturing process of a tufted stack of composite reinforcements.

Tufting technology was primarily devised for making carpet and warm clothing and is being used as an effective technique for reinforcing composite preforms containing multiple layers [5]. The tufting process is illustrated in Fig.1. A hollow needle is employed as the tufting needle, which carries the tufting thread totally or partially through the thickness of the multilayer stack of composite reinforcements.

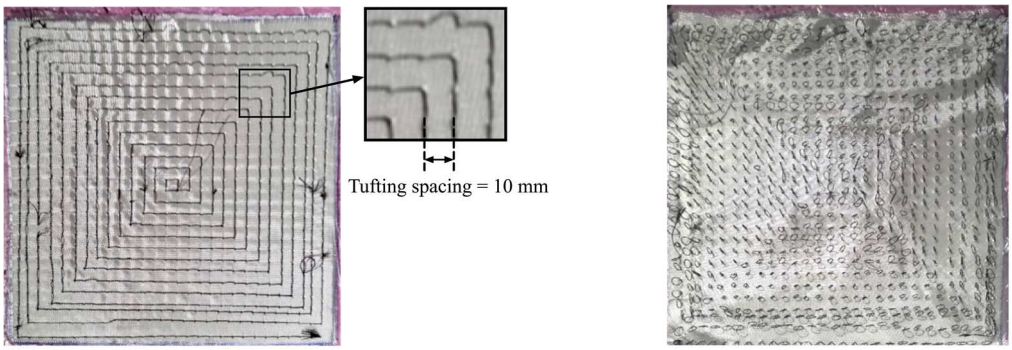

(a) (b)

Fig.2 Tufted stack of composite reinforcements in the initial configuration [16].

Unlike the prevalent stitching procedure, the insertion of tufting thread is tensionless, minimizing the destruction of reinforcements caused by the needle. After the insertion is made, the tufting needle reaches a sacrificial foam at the bottom and is then withdrawn upwards to form a loop. Thanks to the friction force, tufting threads are maintained by tufting holes, and the layers of reinforcement are therefore connected simultaneously.

A multilayer tufted stack of plane textile reinforcements manufactured by GEMTEX laboratory is considered in the present study [16]. The dimensions of this stack are $280\times280\ \mathrm{mm}^2$ with four plies of E-glass plain weave, and the lay-up configuration is $[0°/90°, \pm 45°]_2$. This specimen was tufted with carbon thread in the pattern of a square spiral. The spacing between tufting points is 10 mm (Fig.2). The principal properties of the reinforcement and the tufting thread are listed respectively in Table 1 and Table 2.

Table 1. Principal plain weave reinforcement parameters [23].

	Properties	Units
Weave style	Plain weave	
Area density	160	g/m^2
Type of yarn	Glass-EC968	
Warp	11.8	Yarns/cm
Weft	10.7	Picks/cm
Weight distribution	Warp: 52 Weft: 48	%
Thickness	0.135	mm

Table 2. Principal tufting thread parameters [28].

	Properties	Units
Reference	Tenax®-J HTA-40	
Linear density	2×67	Tex

Number of filaments	2×1000	
Twist	240±16	T/m
Young's modulus per filament	240	GPa
Density per filament	1.77	g/cm^3
Diameter per filament	7	μm

3. Modeling of tufted preform during forming

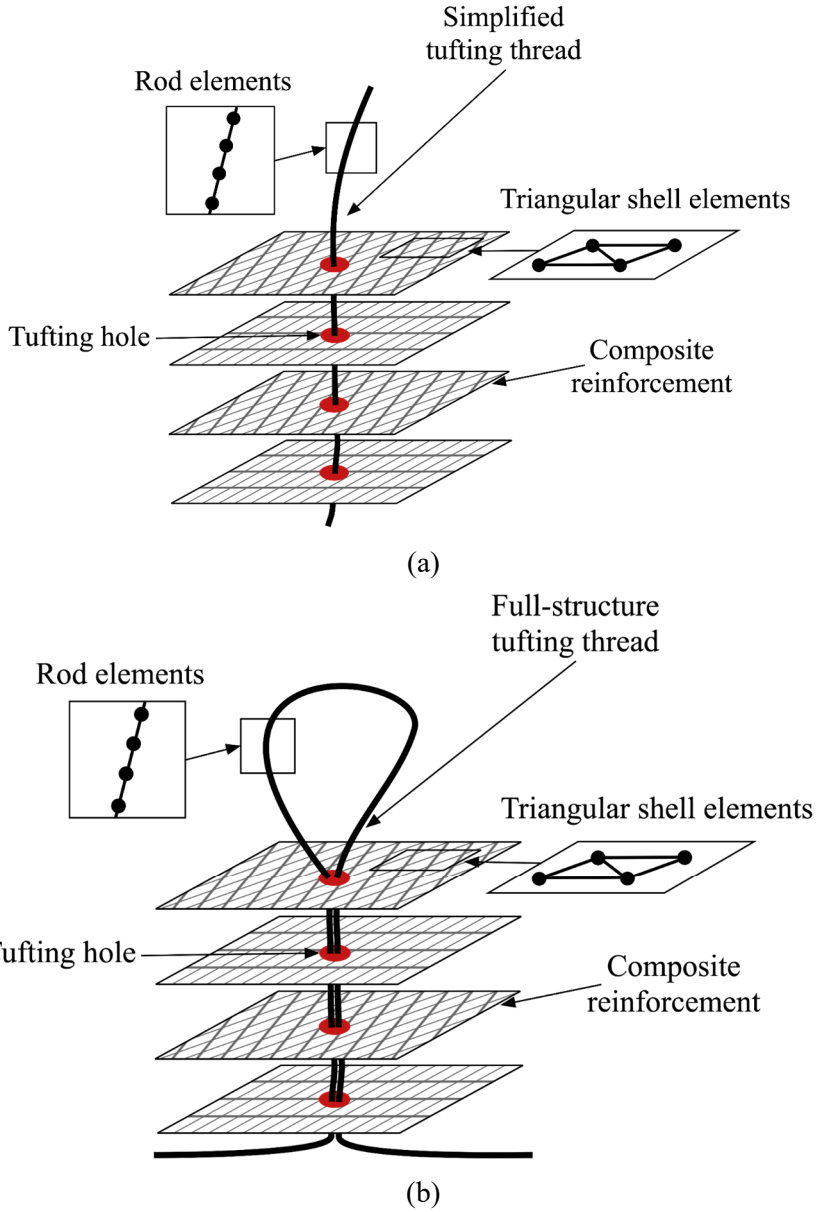

Fig. 3 (a) Simplified model of the tufting (Model I) and (b) full-structure model of the tufting (Model II).

Unlike the stitched preform where the layers are closely linked, the tufting technique keeps the layers connected by fibrous thread, but this connection is not absolutely firm which relies on the friction between threads and holes. The modeling of tufting will therefore be

different from the existing modeling approaches for stitching and NCF [24-27,29-30].

Two models of the tufting are developed in the present study: a simplified model of the tufting (Fig.3a) and a full-structure model of the tufting (Fig.3b), denoted as Model I and Model II, respectively. The tufting thread is represented by rod elements and the composite reinforcement is modeled by shell elements. The tufting hole can be positioned anywhere in the shell element. A sliding-thread contact algorithm manages the interaction and relative movements between the tufting hole and the tufting thread. Model I only considers the through-thickness part of tufting thread, which makes it possible to reduce the number of finite elements required for the simulation and thus the time required for the calculation. Model II takes into account the entire tufting thread, allowing a complete simulation of the deformation of the tufting thread. Model II makes it possible to consider the interactions between neighboring tufting points but it requires more finite elements and longer computation time than Model I.

3.1 Modeling of reinforcements: stress resultant element

A stress resultant shell element [31] is used for the purpose of modeling textile reinforcements. The virtual work theorem relates the external, internal and acceleration virtual works in any kinematically admissible virtual displacement.

$$\delta W_{ext} - \delta W_{int} - \delta W_{acc} = 0 \tag{1}$$

Where δW_{ext} is the external virtual work, δW_{int} is the internal virtual work and δW_{acc} is the acceleration virtual work. Fig.4a shows the stress resultants on a woven unit cell that express the stresses contained in the textile reinforcement, they are the tensions T^{11} and T^{22} along the warp and weft directions, the bending moments M^{11} and M^{22} along the warp and weft directions, and the in-plane shear moment C_γ.

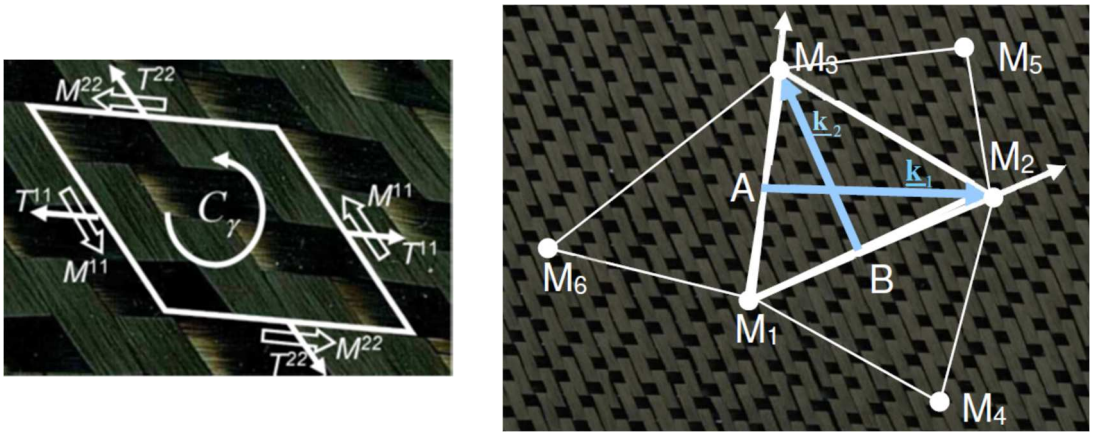

(a) (b)

Fig.4 Stress resultant element: (a) stress resultants on a woven unit cell; (b) shell finite element made of woven unit cell.

The virtual internal work consists of the works of tension δW_t, bending δW_b, and in-plane shear δW_s and can be written as:

$$\delta W_{int} = \delta W_t + \delta W_b + \delta W_s = \sum_{P=1}^{ncell} {}^P\delta\varepsilon_{11}\,{}^PT^{11}\,{}^PL_1 + {}^P\delta\varepsilon_{22}\,{}^PT^{22}\,{}^PL_2 + \sum_{P=1}^{ncell} {}^P\delta\chi_{11}\,{}^PM^{11}\,{}^PL_1 + {}^P\delta\chi_{22}\,{}^PM^{22}\,{}^PL_2 + \sum_{P=1}^{ncell} {}^P\delta\gamma\,{}^PC_\gamma \tag{2}$$

In Eq. (2), P represents the woven unit cell number and $ncell$ is the total number of woven cells in the textile reinforcement. L_1 and L_2 are the woven unit cell lengths in the warp and weft directions. $\delta\varepsilon_{11}$, $\delta\varepsilon_{22}$, $\delta\chi_{11}$, $\delta\chi_{22}$ are respectively the virtual axial strains and bending curvatures in the warp and weft directions of the textile reinforcement, and $\delta\gamma$ is its virtual in-plane shear angle. The tensions $T^{11}(\varepsilon_{11})$ and $T^{22}(\varepsilon_{22})$, the bending moments $M^{11}(\chi_{11})$ and $M^{22}(\chi_{22})$, and the in-plane shear moment $C_\gamma(\gamma)$ describe the mechanical behavior of the textile reinforcement. The formulation of this shell element (Fig.4b) is detailed in [31,32].

3.2 Modeling of the tufting hole

The tufting hole is modeled by an intersection point between a rod chain and a shell element (Fig.5), which satisfies:

$$(\mathbf{L}_{\mathrm{AB}}(t)-\mathbf{p}_0)\cdot\mathbf{n}=0 \tag{3}$$

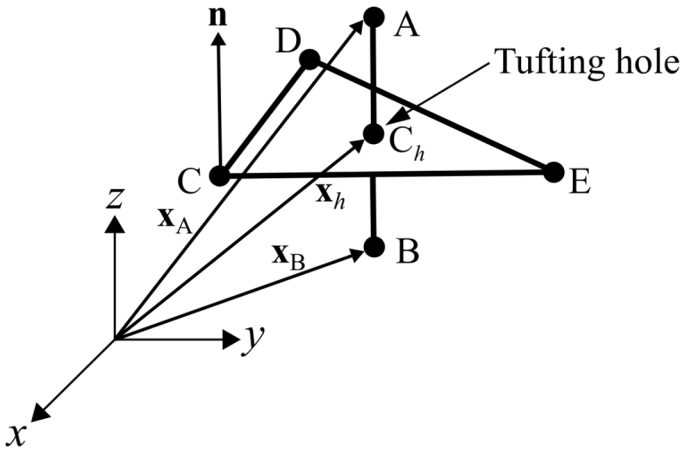

Fig.5 Shematic diagram of the modeling of the tufting hole.

In Eq.(3), $\mathbf{L}_{\mathrm{AB}}(t)=\mathbf{x}_{\mathrm{A}}+t(\mathbf{x}_{\mathrm{B}}-\mathbf{x}_{\mathrm{A}})$ is a parametric equation representing the rod element, $\mathbf{p}_0$ is an arbitrary point in the shell element, and $\mathbf{n}$ is a normal vector to the plane of the shell element. The position of the tufting hole can be obtained by solving for the parameter t:

$$t=\frac{(\mathbf{p}_0-\mathbf{x}_{\mathrm{A}})\cdot\mathbf{n}}{(\mathbf{x}_{\mathrm{B}}-\mathbf{x}_{\mathrm{A}})\cdot\mathbf{n}} \tag{4}$$

The position of the tufting hole is defined in the initial state. It is fixed in the reference element.

3.3 Modeling of the tufting thread

The tufting thread is discretized by rod elements. A "digital rod element" has been initially utilized for the modeling of the fibers [33], and is used in different cases [34-36]. However, the discontinuities of the contact zone of the chain of rod elements can lead to divergence of the simulation. Therefore, it is important to enrich this element for the simulation of the tufted preform.

3.3.1 3D thread smoothing

Previous studies [37,38] have proposed to interpolate a Hermite curve between adjoining rod or beam elements for stabilizing the contact calculation. In the present study, a 3D Hermite curve with C_1-continuity is used to ensure the smooth sliding of the rod chain from the tufting

hole (Fig.6).

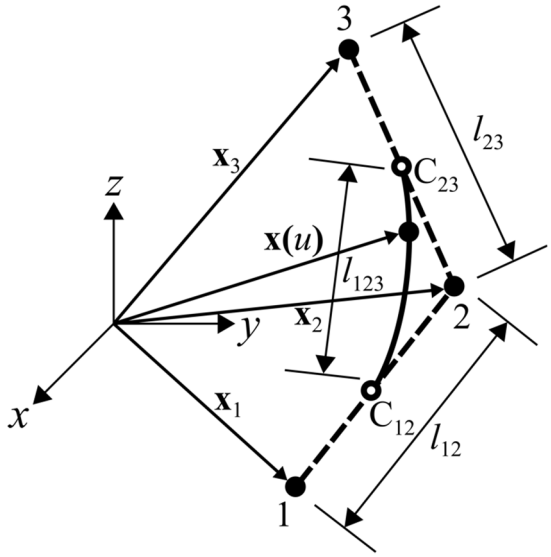

Fig.6 Smoothed contact zone of the rod chain in 3D.

A 3D Hermite interpolation curve can be defined by the function of a parameter u in its local coordinate:

$$\mathbf{x}(u)=\begin{bmatrix} u^3 & u^2 & u & 1 \end{bmatrix}\begin{bmatrix} 2 & -2 & 1 & 1 \\ -3 & 3 & -2 & -1 \\ 0 & 0 & 1 & 0 \\ 1 & 0 & 0 & 0 \end{bmatrix}\begin{bmatrix} \mathrm{C}_{12} \\ \mathrm{C}_{23} \\ \mathrm{dC}_{12} \\ \mathrm{dC}_{23} \end{bmatrix}, u\in[0,1] \tag{5}$$

Where C_{12} and C_{23} are the central positions of the adjacent rod elements, dC_{12} and dC_{23} are their slopes. They can be formulated as follows:

$$\mathrm{C}_{12}=\frac{\mathbf{x}_1+\mathbf{x}_2}{2}, \mathrm{C}_{23}=\frac{\mathbf{x}_2+\mathbf{x}_3}{2}, \mathrm{dC}_{12}=\frac{\mathbf{x}_2-\mathbf{x}_1}{2l_{12}}l_{123}, \mathrm{dC}_{23}=\frac{\mathbf{x}_3-\mathbf{x}_2}{2l_{23}}l_{123} \tag{6}$$

The lengths of the straight segments given in Eq.(6) are determined as follows:

$$l_{12}=\left\|\mathbf{x}_2-\mathbf{x}_1\right\|, l_{23}=\left\|\mathbf{x}_3-\mathbf{x}_2\right\|, l_{123}=\left\|\frac{\mathbf{x}_1+\mathbf{x}_2}{2}-\frac{\mathbf{x}_2+\mathbf{x}_3}{2}\right\| \tag{7}$$

3.3.2 Bending of the tufting thread

Although the bending stiffness of a tufting thread is low, it is necessary to take it into account for a high-quality modeling. A rotation-free bending model [39] is chosen. The curvature of two adjacent rod elements can be calculated by

$$\chi = 2\frac{\sin\varphi}{d} \tag{8}$$

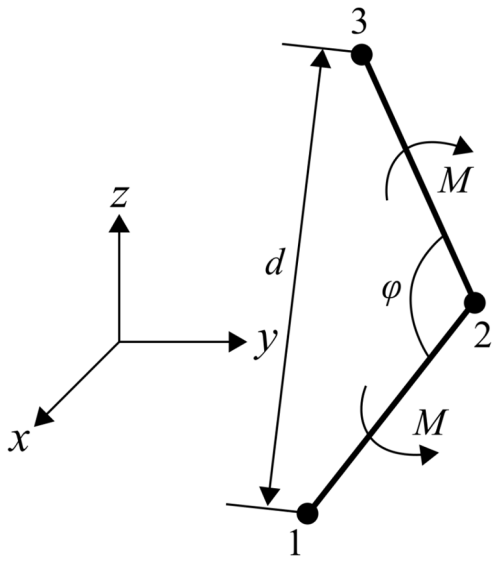

Fig.7 Bending of the tufting thread.

Where φ is the angle between two adjacent rod elements and d is the distance between the node 1 and the node 3.

The moment-curvature behavior of the tufting thread is assumed to be linear:

$$M = G\chi \tag{9}$$

Where G is the bending stiffness of the tufting thread.

Due to this addition of bending stiffness, the rod elements in fact become beam elements.

3.4 Sliding-thread contact algorithm

The slippage between the layers of reinforcements can drive the sliding of tufting threads in tufting holes [16-20]. The penalty method is applied to model the contact interaction between threads and holes. This method is easy to implement to a finite element code and is computationally efficient. Tufting threads can be limited by tufting holes through a node-to-segment (NTS) contact condition until they slip out. A “stick and slip” friction model is used to manage the sliding of the tufting threads. To guarantee a large sliding, a contact detection and a contact release algorithm have been equally developed.

3.4.1 Normal contact

Tufting threads are constrained within tufting holes. A NTS contact condition ensures this restriction by minimizing the orthogonal clearance between the tufting hole and the tufting thread (Fig.8a).

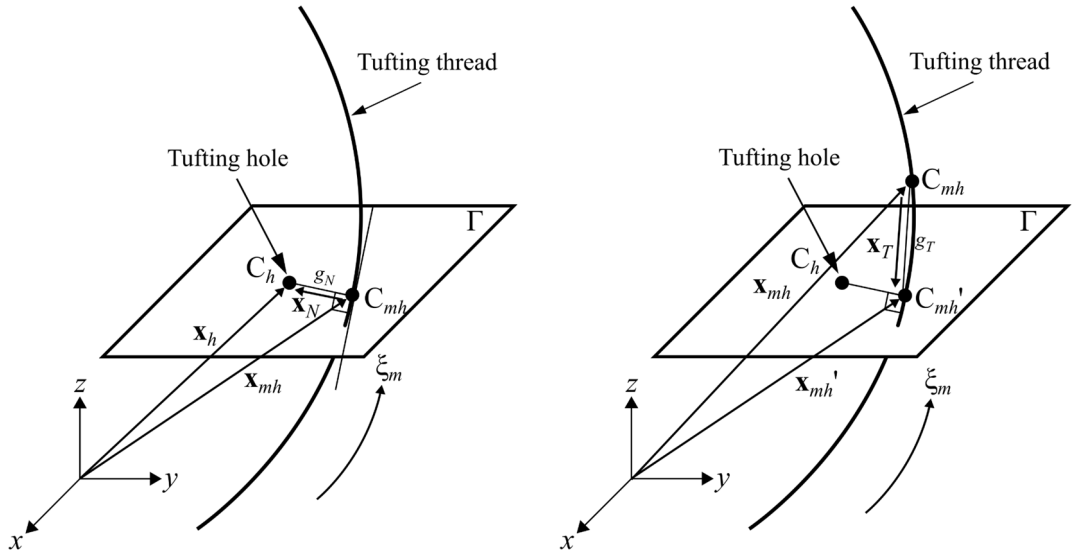

Fig.8 Contact handling: (a) normal gap; (b) tangential gap actualize.

The normal vector $\mathbf{x}_N = \mathbf{x}_h - \mathbf{x}_{mh}$ must be perpendicular to the Hermite interpolation curve of the rod chain (Eq. (5)) and meet the orthogonality condition:

$$\mathbf{x}_N \cdot \frac{\partial \mathbf{x}(u)}{\partial u} = 0 \tag{10}$$

Thus, the orthogonal clearance can be written by:

$$g_N = \left\| \mathbf{x}_N \right\| \tag{11}$$

The normal contact force is obtained by the penalty method and ensures the restriction effects of the tufting hole:

$$\left\| \mathbf{F}_N \right\| = k_N g_N \tag{12}$$

Where k_N is the penalty stiffness of the normal contact.

3.4.2 Tangential contact: friction model

The friction law between tufting threads and tufting holes is expressed in a “stick and slip” form:

$$\text{if } \|\mathbf{F}_T\| - \|\mathbf{F}_f\| < 0, \text{ then } v_T = 0$$
$$\text{if } \|\mathbf{F}_T\| - \|\mathbf{F}_f\| = 0, \text{ then } v_T \geq 0 \tag{13}$$

Where $\mathbf{F}_T$ is the tangential contact force, $\mathbf{F}_f$ is the force of sliding threshold, and v_T is the relative tangential velocity between tufting holes and tufting threads.

The tangential contact force relies on the actual stage of friction, which is adhesion or sliding. In the adhesion stage, the tangential contact force can be represented, in a method of penalty:

$$\|\mathbf{F}_T\| = k_T g_T \tag{14}$$

Where the tangential gap $g_T = \|\mathbf{x}_T\| = \|\mathbf{x}_{mh'} - \mathbf{x}_{mh}\|$ (Fig.8b) and k_T is the penalty stiffness of the tangential contact.

In the sliding stage, the tangential force needs to be actualized:

$$\|\mathbf{F}_T\| = \|\mathbf{F}_f\| \tag{15}$$

The experimental identification of the sliding threshold $\|\mathbf{F}_f\|$ will be presented in the Section 3.5.

3.4.3 Contact detection: determination of the active node

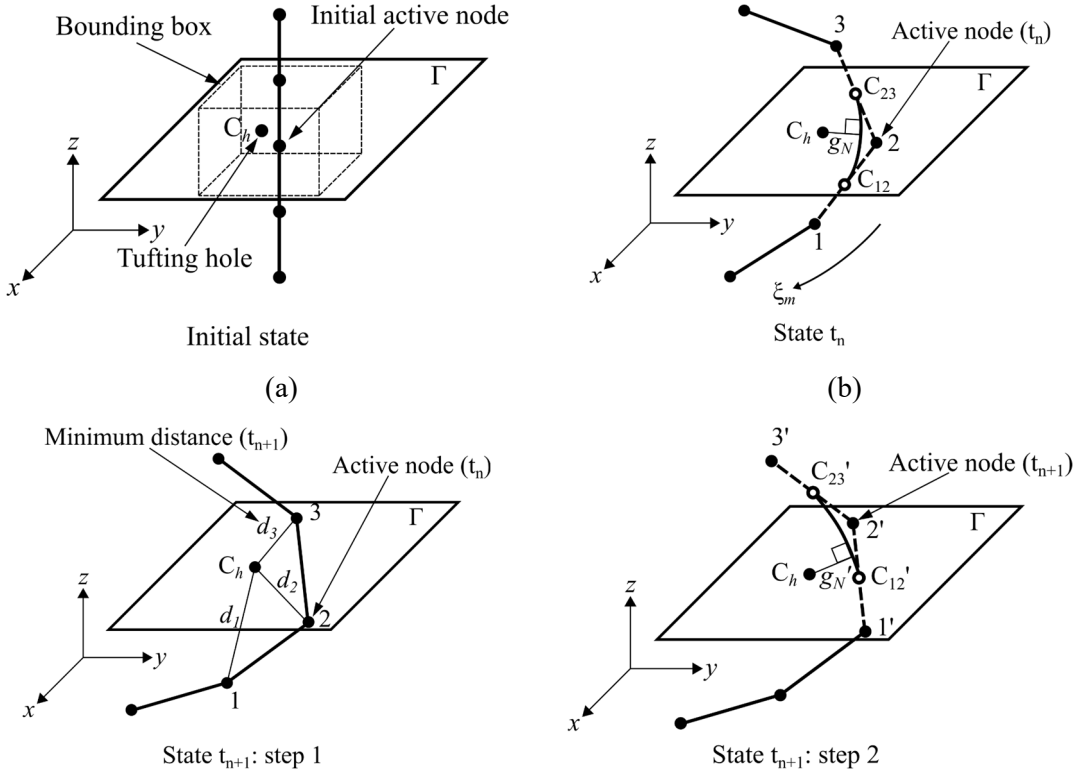

(c) (d)

Fig.9 Determination of the active node: (a) initial state: search for the initial active node by a bounding box; (b) state t_n: contact calculation with the active node (node 2); (c) step 1 of the state t_{n+1}: search the node with the minimum distance to the tufting hole; (d) step 2 of the state t_{n+1}: contact calculation with the new active node (node 2').

Before launching the calculation of contact forces for each timestep, it is necessary to find the active node. A typical algorithm of contact detection has to loop all nodes found in a bounding box and to be repeated during the simulation [40]. In order to reduce computation time, as well as to find the correct active node, an algorithm that combines a detection of the bounding box and a distance comparison of neighboring nodes, is developed (Fig.9). This algorithm consists of the following steps:

(1) In the initial state t_0, the first active node is found by searching in the bounding box established around the tufting hole (Fig.9a). Then, this node will be stored by the program so that the next state can recall it;

(2) When the state changes from t_n (Fig.9b) to t_{n+1}, the active node for contact calculation must be updated. The distance between the tufting hole and the active node (d_2), and the distances between the tufting hole and two other neighboring nodes (d_1 and d_3) will be compared (Fig.9c). Once the node with the minimum distance is found, the corresponding node will be considered as the new active node (Fig.9d).

Using this detection algorithm, the active node candidates for each tufting point per time step was reduced from 100 nodes to only three nodes (the active node and its two neighboring nodes), making the detection process more efficient. Moreover, the storage of the active node at each time step avoids erroneous detections when the active node candidates are extremely close.

3.4.4 Sliding continuity of the tufting thread

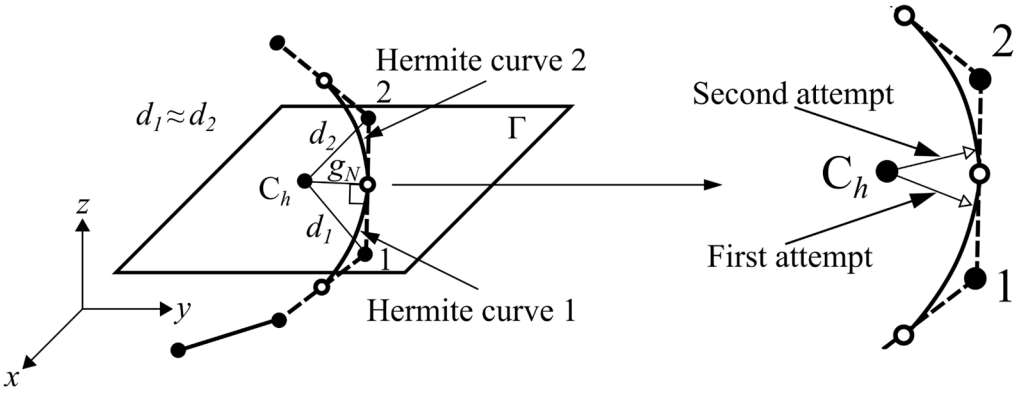

Fig.10 Management of the continuity of sliding.

Fig.10 shows a special case where the tufting hole C_h is facing the transition zone of two neighboring Hermite curves, a tiny difference between d_1 and d_2 (order of 10^{-4}) will cause the tufting hole to have no orthogonal solution on the Hermite interpolation curve. A method of double attempt is needed in order to deal with this challenging situation. If there is no solution in a first attempt, the algorithm will pass the active node from node 1 to node 2 and then make a second attempt on the Hermite curve 2. Finally, a solution that satisfies the orthogonal condition (Eq. (10)) will undoubtedly be found thanks to the C_1-continuity of the Hermite interpolation curve.

3.4.5 Contact release: exit of the tufting thread

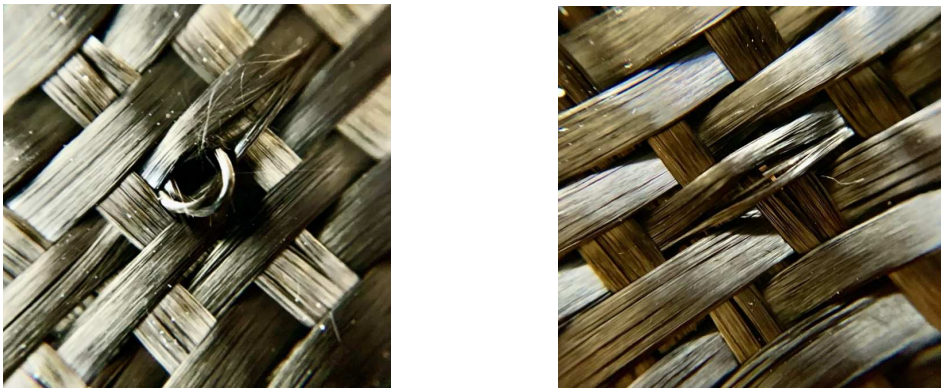

(a) (b)

Fig.11 Exit of the tufting thread: (a) partial exit; (b) total exit.

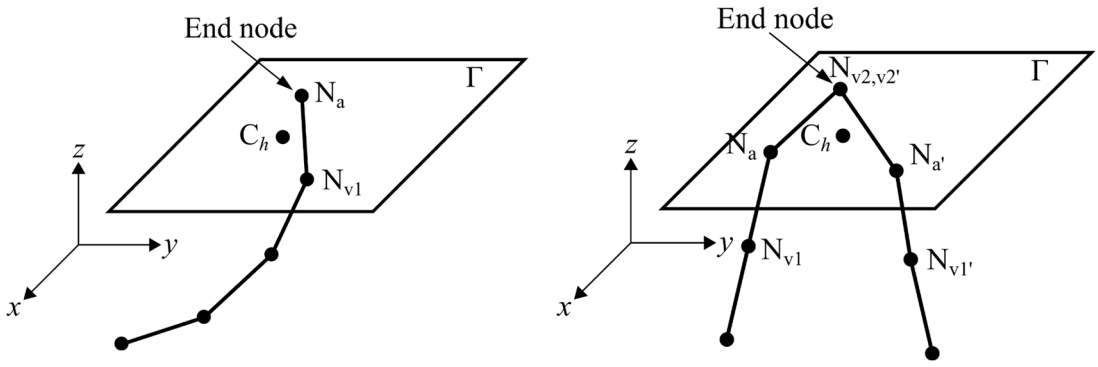

(a) (b)

Fig.12 Contact release for Model I (a) and Model II (b).

Tufting threads have the possibility to slip out of tufting holes as inter-ply sliding increases during the forming process (Fig.11). The exit of the tufting thread can be treated numerically as an equivalence to the release of the contact algorithm. For Model I, the contact algorithm is disabled under the condition that there is only one adjacent node to the active node (Fig.12a). For Model II, the contact algorithm is stopped when the active node of each thread has a common neighboring node (Fig.12b).

3.5 Friction parameter identification

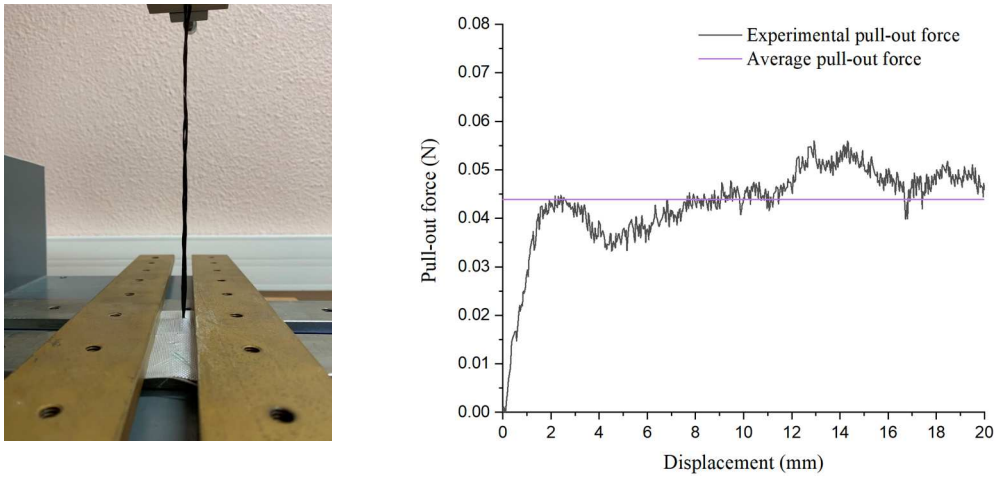

(a) (b)

Fig.13 Single thread pull-out test: (a) experimental setup; (b) load–displacement curve.

The sliding threshold $\|\mathbf{F}_f\|$ between tufting threads and tufting holes was measured by a simple pull-out test. The tested thread was not subjected to any external force other than tensile force. By utilizing the experimental setup in Fig.13a, the in-plane shear and the axial tension of the textile reinforcement were minimized. The thread was pulled vertically out of the

reinforcement by a traction machine at a speed of 10.0 mm/min, and a high-precision load sensor (10N-sensor) was used. A reproducible load-displacement curve was obtained (3 pull-out tests) and shown in Fig.13b. The sliding force can be considered constant according to the load-displacement curve. The average sliding force is 0.044 ± 0.008 N.

4. Numerical investigation

4.1 Basic numerical tests

The numerical tests presented in this section are chosen to show the effectiveness of the developed models of tufting (Model I and Model II). In these tests, tufting threads slide with the movement of reinforcements. This sliding does not rely on external forces, and it is only achieved by the contact forces between them.

4.1.1 Test 1: tufted four-layer stack using Model I

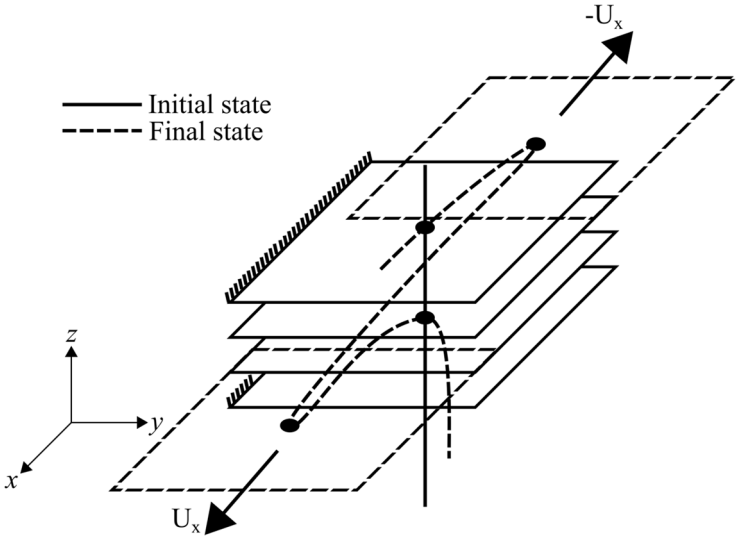

(a)

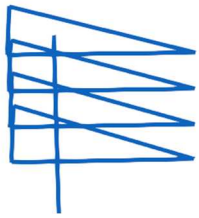

(b)

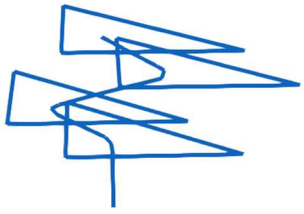

(c)

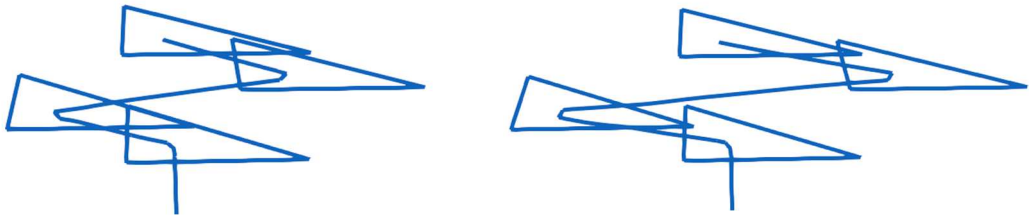

(d) (e)

Fig.14 Test 1: (a) boundary condition; (b) Initial state; (c) 33% of the displacement; (d) 66% of the displacement; (e) 100% of the displacement.

The length of the tufting thread is 20 mm. The tufting thread is discretized with 200 rod elements and the multilayer stack of composite reinforcements is represented by four triangular shell elements. The mechanical properties of the tufting thread and the connected plies are presented in Table 3 and Table 4. Fig.14b, c, d and e show that the deformation of the tufting thread follows the trajectory of the layers' movement with stability, especially when the angle between the thread and the reinforcement is important (Fig.14e).

4.1.2 Test 2: tufted four-layer stack using Model II

The tufting thread is modeled in its entirety, including the loop and the in-plane thread. In this test, two distinct stacks of reinforcements have a relative movement and are connected by an in-plane tufting thread (Fig.15a). The complexity of the numerical model is augmented by taking into account the in-plane thread.

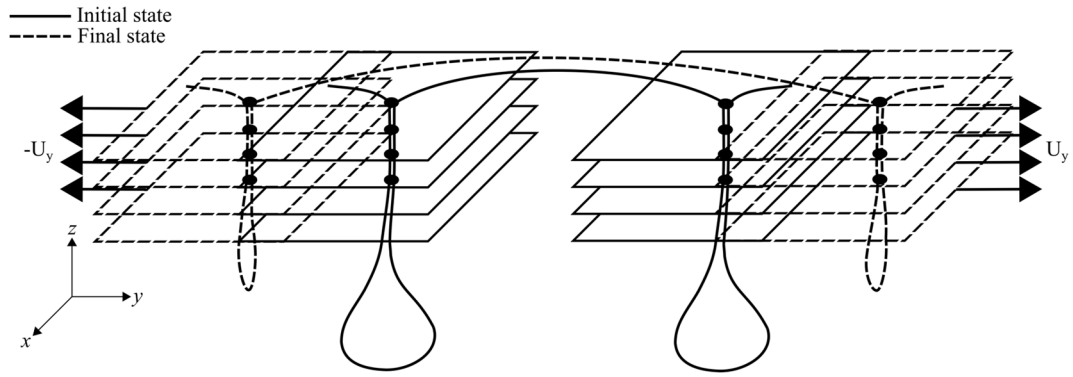

(a)

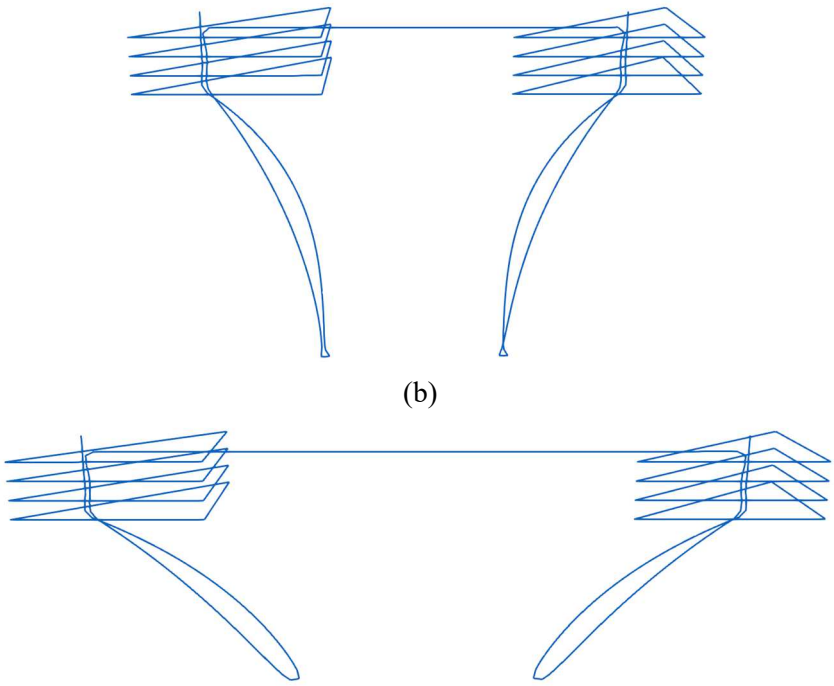

(b)

(c)

Fig.15 Test 2: (a) boundary condition; (b) 50% of the displacement; (c) 100% of the displacement.

However, the detailed deformation of the tufting thread can be fully presented by Model II. Fig.15b and c show that the in-plane thread is stretched as the two sides of the fabric move away from each other, while the loops are getting shorter. This test proves the ability of Model II to handle complex contacts between tufting threads and tufting holes.

4.2 Forming simulations using Model I

To demonstrate and validate the model of tufting developed in the present study, a hemisphere forming and a square-box forming were simulated and compared to forming experiments.

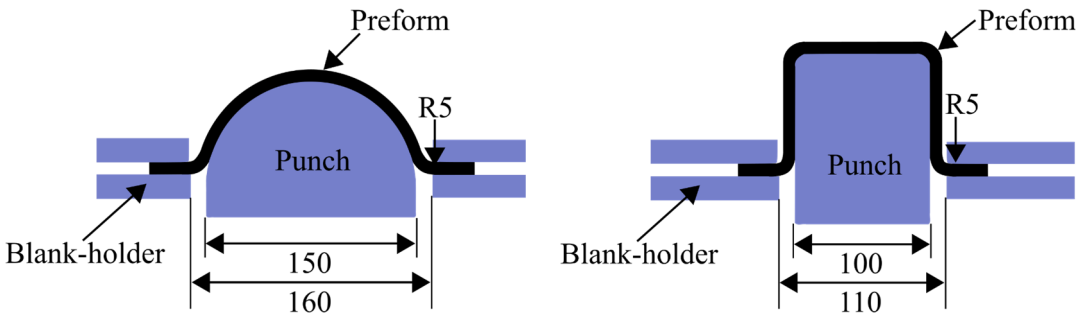

(a) (b)

Fig.16 Forming device: (a) hemispherical forming (b) square box forming (unit: mm).

The forming device is in Fig.16 [16-20]. The tufted stack of four composite reinforcements layers shown in Fig.2 was shaped in hemispherical punch and square box punch. Each layer is composed of a balanced plain-weave fabric (E-glass). The mechanical properties for this reinforcement have been characterized previously [23] (Table 3). To illustrate the influence of tufting threads on the forming results, the same stack but without tuft is formed and simulated. Table 4 shows the mechanical properties of the tufting thread. The bending stiffness of the tufting thread is calculated following the approach given in [41].

As Model I does not consider the in-plane tufting thread, the tufted preform is symmetric that only requires to model one quarter of the structure. The simulation involves 147913 shell elements and 38808 rod elements. The size of the shell element was set to 1.5 mm for a good representation of the wrinkling phenomenon. The total length of the tufting thread through the thickness including the loop is 20 mm. Each inserted tufting thread is represented by 200 rod elements. Computation times ratio between the forming simulation of tufted/non-tufted preform is approximately 1.5.

Table 3. Mechanical properties of the reinforcement.

Mechanical properties		Units
Tension $T^{11}=C_1\varepsilon_{11}; T^{22}=C_2\varepsilon_{22}$	$C_1 = C_2 = 1000$	N/Yarn
In-plane shear $C_\gamma=K_1\gamma+K_2\gamma^3+K_3\gamma^5$	$K_1 = 0.371$ $K_2 = -0.841$ $K_3 = 1.013$	Nmm
Bending $M^{11}=B_1\chi_{11}$; $M^{22}=B_2\chi_{22}$	$B_1 = B_2 = 0.10$	Nmm
Friction		
Ply-to-ply (Coulomb coefficient)	0.21	
Tool-to-ply (Coulomb coefficient)	0.23	

Table 4. Mechanical properties of the tufting thread.

Mechanical properties		Units
Tension $T=E\varepsilon$	E=11666	N/Thread
Bending $M = G\chi$	$G = 0.056$	$\mathrm{N\,mm^2}$

4.2.1 Hemispherical forming

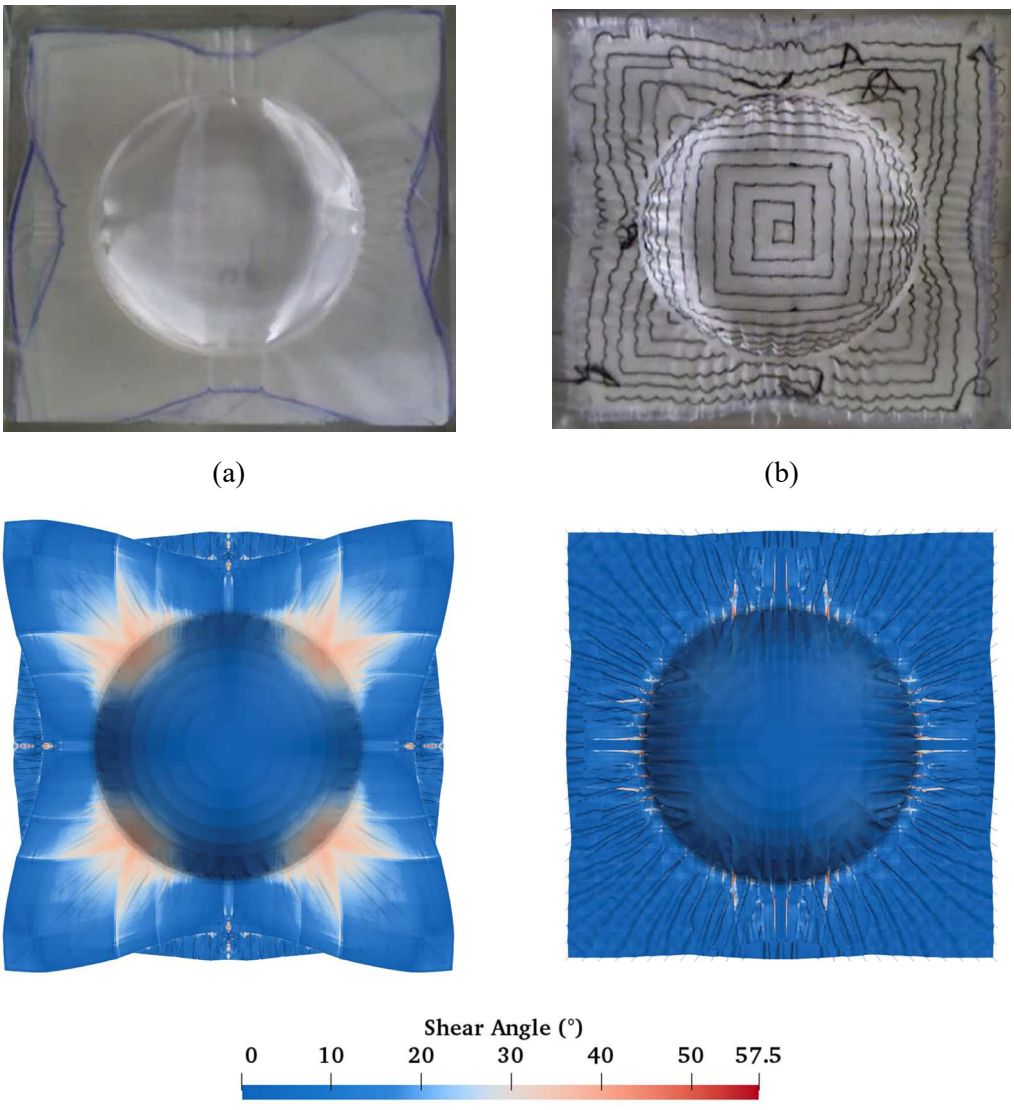

Fig.17 Deformation of the non-tufted preform and the tufted preform after the hemispherical forming: experiments (a) and (b) [16] and simulations (c) and (d).

Fig.17 shows that there are smaller differences between the deformations of differently oriented layers in the tufted preform than in the preform without tuft. Due to the tufting thread inserted within the preform, the inter-ply sliding and the material draw-in have been reduced. Comparison for the formed profiles in experiment and simulation is presented in Fig.18, and they are in good agreement. The distribution of the wrinkles in the punch zone is more homogenous (Fig.19). The tufting threads block the propagation of the wrinkles, making them occur mainly between the tufting points. A comparison of the wrinkle height in experiment and simulation is given in Table 5, which shows a correct agreement.

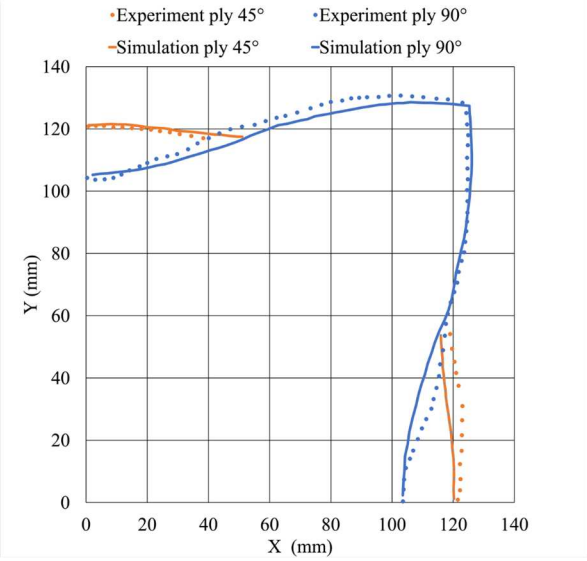

(a)

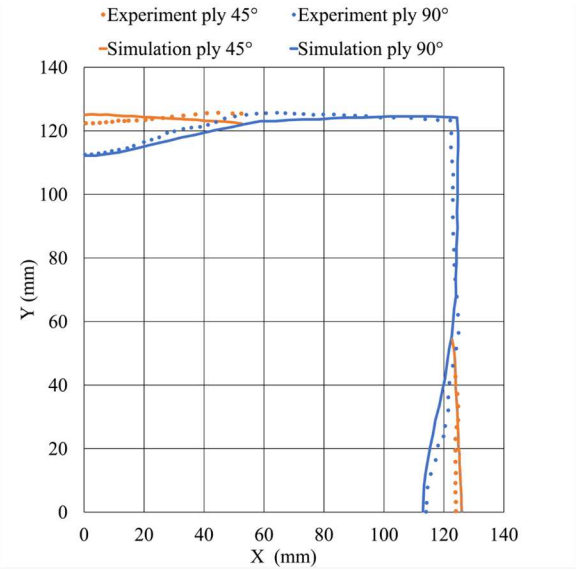

(b)

Fig.18 Comparison of the formed profiles between experiment and simulation for the non-tufted preform (a) and the tufted preform (b).

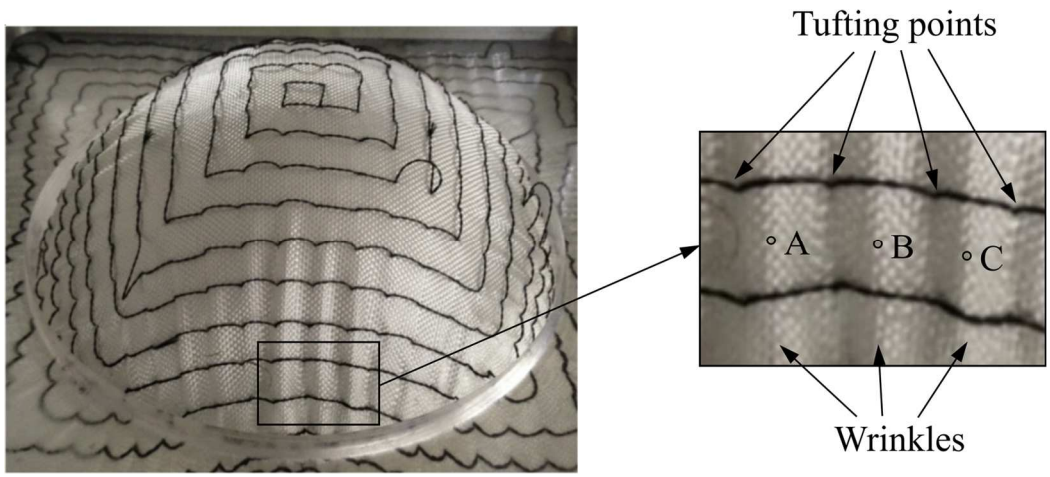

(a)

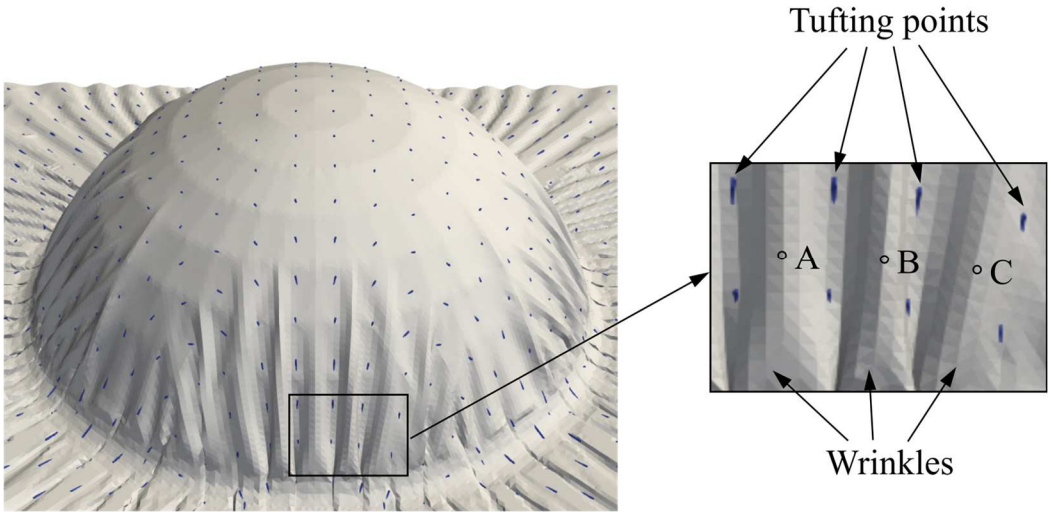

(b)

Fig.19 Wrinkles of the tufted preform in the hemispherical forming: (a) experiment [16]; (b) simulation.

Table 5. Comparison of the wrinkle height in experiment and simulation the hemispherical forming (mm)

	h_A	h_B	h_C	$h_{average\text{-}tufted}$	$h_{average\text{-}non\ tufted}$
Experiment	2.8	1.9	2.4	2.37	2.54
Simulation	2.2	2.5	2.3	2.33	2.35

4.2.2 Square box forming

The forming on a square box is more difficult than on a hemisphere, and severe wrinkles can occur during the forming process [42]. The experimental square box forming for multilayer stack of composite reinforcements reinforced by tufting has been studied by Shen et al. [17].

Similar to the hemispherical forming, the forming and the wrinkles are modified by tufting threads in the square box forming (Fig.20). The simulated wrinkling phenomenon of the tufted preform matches that of the experimental one (Fig.21). Furthermore, the wrinkle height is correctly captured by the simulation (Table 6).

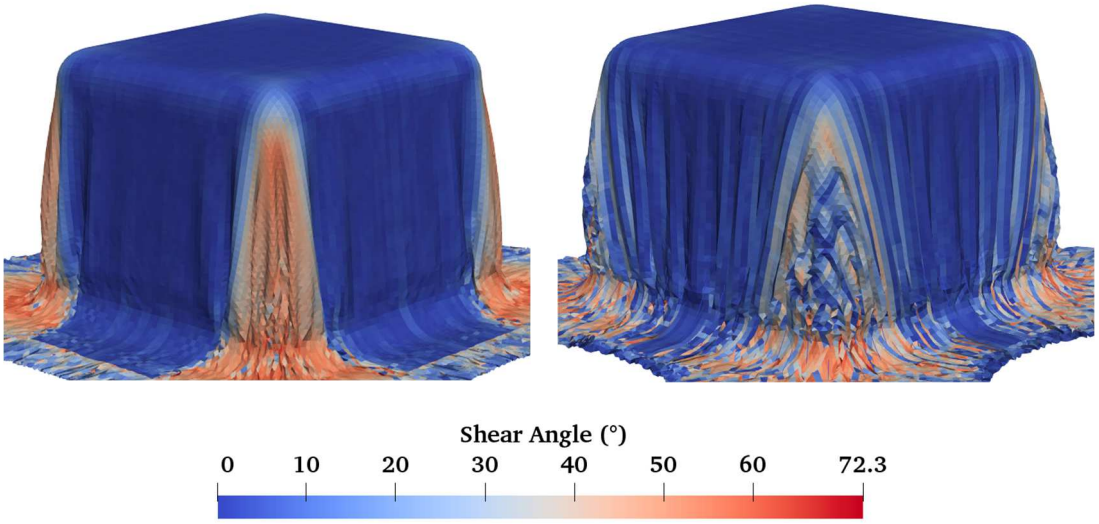

(a) (b)

Fig.20 Shear angle distributions of (a) a non-tufted preform and (b) a tufted preform with four plies after the square box forming.

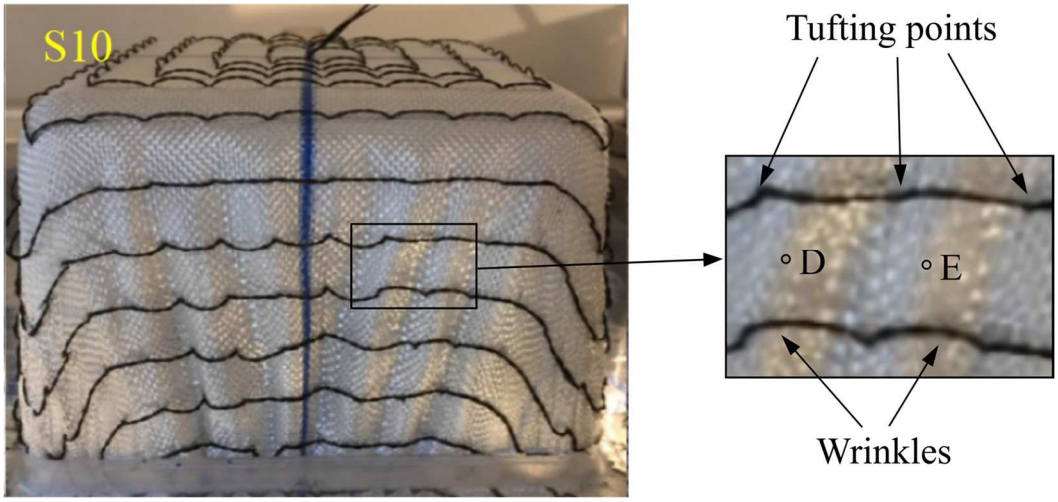

(a)

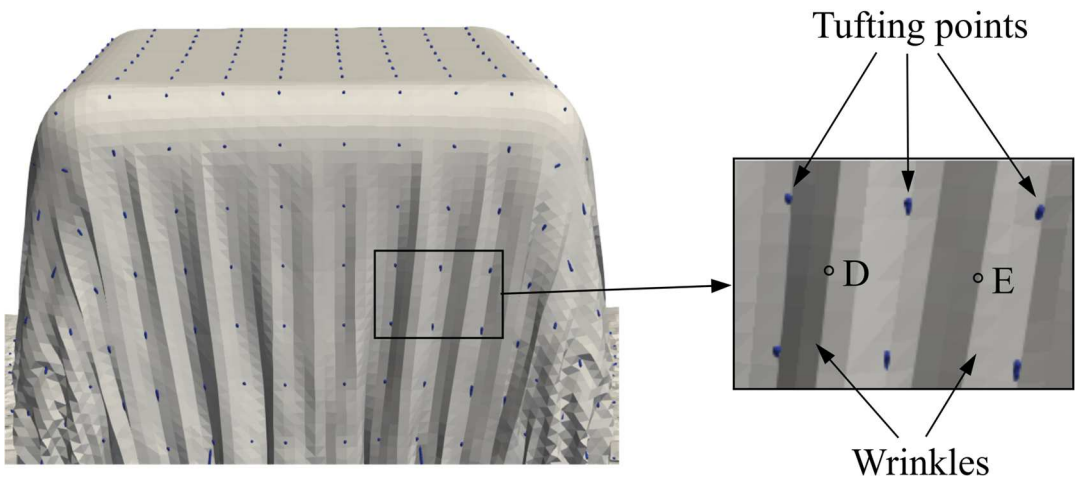

(b)

Fig.21 Wrinkles of the tufted preform in the square box forming: (a) experiment [17]; (b) simulation.

Table 6. Comparison of the wrinkle height in experiment and simulation of the square box forming (mm)

	h_D	h_E	$h_{average\text{-}tufted}$	$h_{average\text{-}non\ tufted}$
Experiment	3.1	2.8	2.95	3.32
Simulation	3.5	2.6	3.05	3.10

4.3 Hemispherical forming simulation using Model II

Model II allows not only the modeling of tufting thread along the thickness direction of the preform but also the in-plane tufting thread between the holes. As the tufting pattern can be asymmetrical, the number of finite elements may increase up to four times compared to Model I. The comparison between experiment and simulation demonstrates that Model II is able to predict the deformed shape of the tufted preform as well as the formation of wrinkles in the punch zone (Fig.22a and b). Furthermore, the predicted deformation of the in-plane tufting thread, which is influenced by the blank-holder, is in good agreement with the experimental results (Fig.22c and d). Model II can also simulate the square box forming with the tufted preform. It would allow in particular to know the position of the threads between the tufting holes.

Model II can be applied to investigate the influence of tufting thread on the in-plane properties of tufted preform. In addition, it is possible to optimize the blank-holder's pressure

by using Modell II. Optimized pressure will reduce the tufting thread's damage induced by the blank-holder.

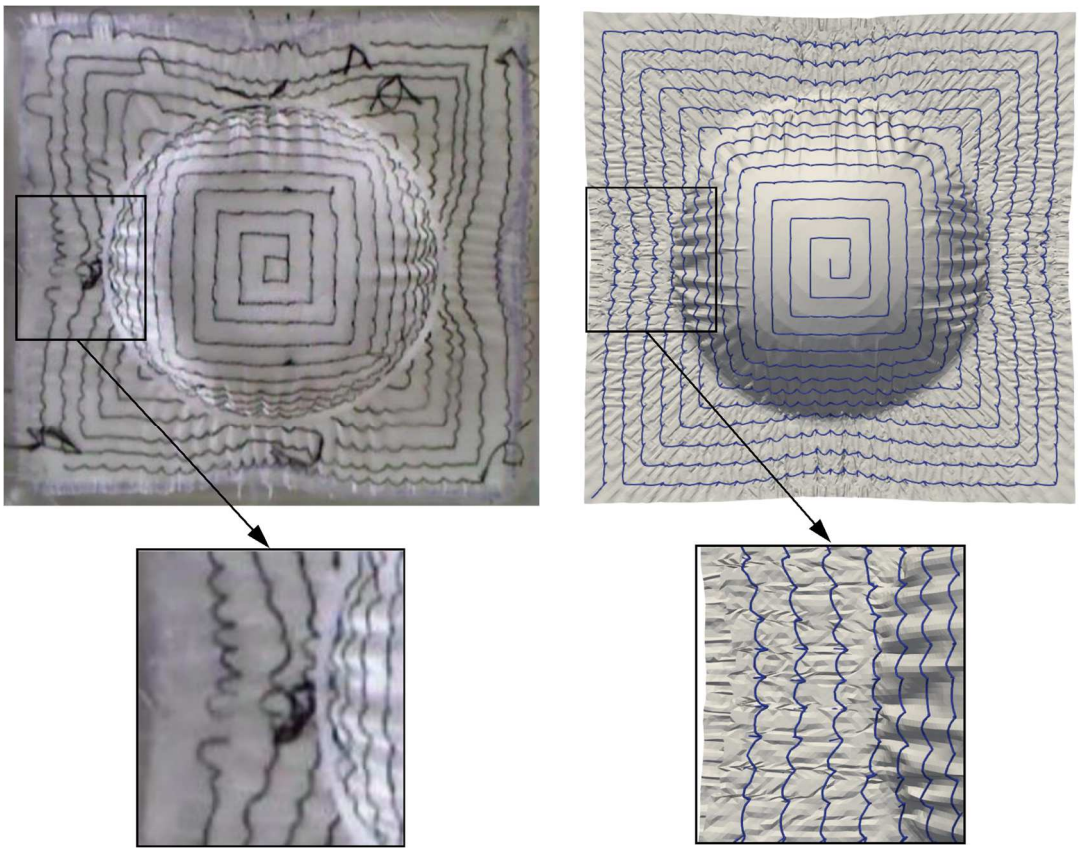

(a) (b)

Fig.22 Deformed shape of the tufted preform and deformation of the in-plane tufting thread in experiment (a) [16] and simulation (b).

5. Conclusions

Modeling of the forming of tufted multilayer textile composite reinforcements has been proposed. The tufting thread is modelized by a chain of rod elements in a simplified (Model I) and complete approach (Model II). The interaction between the tufting thread and the composite reinforcement is handled by a contact normal force accompanying a friction threshold. A C_1-continuous geometry of the rod chain, as well as a sliding-thread contact algorithm have been proposed to ensure a large sliding of the tufting thread in the tufting hole. The bending stiffness of the thread is taken into account.

The proposed models are firstly verified by two basic numerical tests. Then the simulation results of the hemispherical and square box forming are compared with the experimental results. Both Model I and Model II have shown their abilities to simulate the

tufted preform during the forming process. Furthermore, Model II can simulate the stresses/strains in the in-plane tufting threads and their influence on the deformation of the preform. This aspect will need to be explored in more detail in future studies.

The forming of the fibrous reinforcement stacks is modified by the presence of tufting. The position of the tufted areas can be optimized in order to obtain an optimal forming of the stack that minimizes defects and in particular wrinkles. The tufted preform simulation tool will be an important asset to achieve this optimization.

Acknowledgements

This work was supported by Agence Nationale de la Recherche,

grant N° ANR-16-CE08-0042-02 COMP3DRE.

References

[1] Partridge IK, Cartié DDR. Delamination resistant laminates by Z-Fiber® pinning: Part I manufacture and fracture performance. Composites Part A: Applied Science and Manufacturing 2005;36:55–64.

[2] Mouritz AP. Review of z-pinned laminates and sandwich composites. Composites Part A: Applied Science and Manufacturing 2020;139:106128.

[3] Wittig J. Recent development in the robotic stitching technology for textile structural composites. In: Falcone A, Nelson KM, Albers R, Avery WB, editors. Advancing Affordable Materials Technology, vol. 33, 2001, p. 540–50.

[4] Bel S, Boisse P, Dumont F. Analyses of the Deformation Mechanisms of Non-Crimp Fabric Composite Reinforcements during Preforming. Appl Compos Mater 2012;19:513–28.

[5] Dell'Anno G, Treiber JWG, Partridge IK. Manufacturing of composite parts reinforced through-thickness by tufting. Robotics and Computer-Integrated Manufacturing 2016;37:262–72.

[6] Cartié DDR, Dell'Anno G, Poulin E, Partridge IK. 3D reinforcement of stiffener-to-skin T-joints by Z-pinning and tufting. Engineering Fracture Mechanics 2006;73:2532–40.

[7] Hartley JW, Kratz J, Ward C, Partridge IK. Effect of tufting density and loop length on the crushing behaviour of tufted sandwich specimens. Composites Part B: Engineering 2017;112:49–56.

[8] Verma KK, Padmakara G, Gaddikeri KM, Ramesh S, Kumar S, Bose S. The key role of thread and needle selection towards 'through-thickness reinforcement' in tufted carbon fiber-epoxy laminates. Composites Part B: Engineering 2019;174:106970.

[9] Osmiani C, Mohamed G, Treiber JWG, Allegri G, Partridge IK. Exploring the influence of micro-structure on the mechanical properties and crack bridging mechanisms of fibrous tufts. Composites Part A: Applied Science and Manufacturing 2016;91:409–19.

[10] Pappas G, Joncas S, Michaud V, Botsis J. The influence of through-thickness reinforcement geometry and pattern on delamination of fiber-reinforced composites: Part I – Experimental results. Composite Structures 2018;184:924–34.

[11] Bigaud J, Aboura Z, Martins AT, Verger S. Analysis of the mechanical behavior of composite T-joints reinforced by one side stitching. Composite Structures 2018;184:249–55.
[12] Wang Y, Soutis C. A Finite Element and Experimental Analysis of Composite T-Joints Used in Wind Turbine Blades. Appl Compos Mater 2018;25:953–64.
[13] Yan S, Zeng X, Long A. Experimental assessment of the mechanical behaviour of 3D woven composite T-joints. Composites Part B: Engineering 2018;154:108–13.
[14] Verma KK, Viswamurthy SR, Gaddikeri KM, Ramesh S, Kumar S, Bose S. Tufting thread and density controls the mode-I fracture toughness in carbon/epoxy composite. Composite Structures 2020:113272.
[15] Mills AR, Jones J. Investigation, manufacture, and testing of damage-resistant airframe structures using low-cost carbon fibre composite materials and manufacturing technology. Proceedings of the Institution of Mechanical Engineers, Part G: Journal of Aerospace Engineering 2010;224:489–97.
[16] Liu L, Zhang T, Wang P, Legrand X, Soulat D. Influence of the tufting yarns on formability of tufted 3-Dimensional composite reinforcement. Composites Part A: Applied Science and Manufacturing 2015;78:403–11.
[17] Shen H, Wang P, Legrand X, Liu L, Soulat D. Influence of the tufting pattern on the formability of tufted multi-layered preforms. Composite Structures 2019;228:111356.
[18] Shen H, Wang P, Legrand X, Liu L. Characterisation and optimisation of wrinkling during the forming of tufted three-dimensional composite preforms. Composites Part A: Applied Science and Manufacturing 2019;127:105651.
[19] Gnaba I, Legrand X, Wang P, Soulat D. Through-the-thickness reinforcement for composite structures: A review. Journal of Industrial Textiles 2019;49:71–96.
[20] Gnaba I, Soulat D, Legrand X, Wang P. Investigation of the formability behaviour during stamping of tufted and un-tufted carbon preforms: towards localized reinforcement technologies. Int J Mater Form 2021.
[21] Vanclooster K, Lomov SV, Verpoest I. On the formability of multi-layered fabric composites. Proc 17th Int Conf Compos Mater, 2009, p. 1–10.
[22] ten Thije RHW, Akkerman R. A multi-layer triangular membrane finite element for the forming simulation of laminated composites. Composites Part A: Applied Science and Manufacturing 2009;40:739–53.
[23] Guzman-Maldonado E, Wang P, Hamila N, Boisse P. Experimental and numerical analysis of wrinkling during forming of multi-layered textile composites. Composite Structures 2019;208:213–23.
[24] Duhovic M, Mitschang P, Bhattacharyya D. Modelling approach for the prediction of stitch influence during woven fabric draping. Composites Part A: Applied Science and Manufacturing 2011;42:968–78.
[25] Bel S, Hamila N, Boisse P, Dumont F. Finite element model for NCF composite reinforcement preforming: Importance of inter-ply sliding. Composites Part A: Applied Science and Manufacturing 2012;43:2269–77.
[26] Chen S, Endruweit A, Harper LT, Warrior NA. Inter-ply stitching optimisation of highly drapeable multi-ply preforms. Composites Part A: Applied Science and Manufacturing 2015;71:144–56.

[27] Schirmaier FJ, Dörr D, Henning F, Kärger L. A macroscopic approach to simulate the forming behaviour of stitched unidirectional non-crimp fabrics (UD-NCF). Composites Part A: Applied Science and Manufacturing 2017;102:322–35.
[28] Hui C, Wang P, Legrand X. Improvement of tufting mechanism during the advanced 3-dimensional tufted composites manufacturing: To the optimisation of tufting threads degradation. Composite Structures 2019;220:423–30.
[29] Yu W-R, Harrison P, Long A. Finite element forming simulation for non-crimp fabrics using a non-orthogonal constitutive equation. Composites Part A: Applied Science and Manufacturing 2005;36:1079–93.
[30] Bardl G, Nocke A, Hübner M, Gereke T, Pooch M, Schulze M, et al. Analysis of the 3D draping behavior of carbon fiber non-crimp fabrics with eddy current technique. Composites Part B: Engineering 2018;132:49–60.
[31] Hamila N, Boisse P, Sabourin F, Brunet M. A semi-discrete shell finite element for textile composite reinforcement forming simulation. International Journal for Numerical Methods in Engineering 2009;79:1443–66.
[32] Hamila N, Boisse P. A Meso–Macro Three Node Finite Element for Draping of Textile Composite Preforms. Appl Compos Mater 2007;14:235–50.
[33] Wang Y, Sun X. Digital-element simulation of textile processes. Composites Science and Technology 2001;61:311–9.
[34] Miao Y, Zhou E, Wang Y, Cheeseman BA. Mechanics of textile composites: Micro-geometry. Composites Science and Technology 2008;68:1671–8.
[35] Wang Y, Miao Y, Swenson D, Cheeseman BA, Yen C-F, LaMattina B. Digital element approach for simulating impact and penetration of textiles. International Journal of Impact Engineering 2010;37:552–60.
[36] Wang Y, Miao Y, Huang L, Swenson D, Yen C-F, Yu J, et al. Effect of the inter-fiber friction on fiber damage propagation and ballistic limit of 2-D woven fabrics under a fully confined boundary condition. International Journal of Impact Engineering 2016;97:66–78.
[37] Wriggers P, Krstulovic-Opara L, Korelc J. Smooth C1-interpolations for two-dimensional frictional contact problems. Int J Numer Meth Engng 2001;51:1469–95.
[38] Litewka P. Hermite polynomial smoothing in beam-to-beam frictional contact. Comput Mech 2007;40:815–26.
[39] Smoljanović H, Uzelac I, Trogrlić B, Živaljić N, Munjiza A. A computationally efficient numerical model for a dynamic analysis of beam type structures based on the combined finite-discrete element method. Materialwissenschaft Und Werkstofftechnik 2018;49:651–65.
[40] Yastrebov VA. Numerical methods in contact mechanics. John Wiley & Sons; 2013.
[41] Ly NG, Denby EF. Bending rigidity and hysteresis of wool worsted yarn. Textile Research Journal 1984;54:180–7.
[42] Wang P, Legrand X, Boisse P, Hamila N, Soulat D. Experimental and numerical analyses of manufacturing process of a composite square box part: Comparison between textile reinforcement forming and surface 3D weaving. Composites Part B: Engineering 2015;78:26–34.